Supplementary material

Sensors embedded in the device (on the anode stimulation electrode, device center, and cathode stimulation electrode) showed devices quickly (τ = 40 s) warms from room temperature to skin surface temperature (Supplementary Fig. 1a), with an incrementally higher temperature at the cathode (Supplementary Fig. 1c), consistent with enhanced erythema. Associated warming at the skin surface was confirmed by thermal imaging (Supplementary Fig. 1d). We further developed a computational model of device heat transfer (Supplementary Fig. 1b), consistent with experimental findings. These results confirm that the primary temperature increase reflects device warming to body surface temperature, as the case for conventional electrotherapies (27).

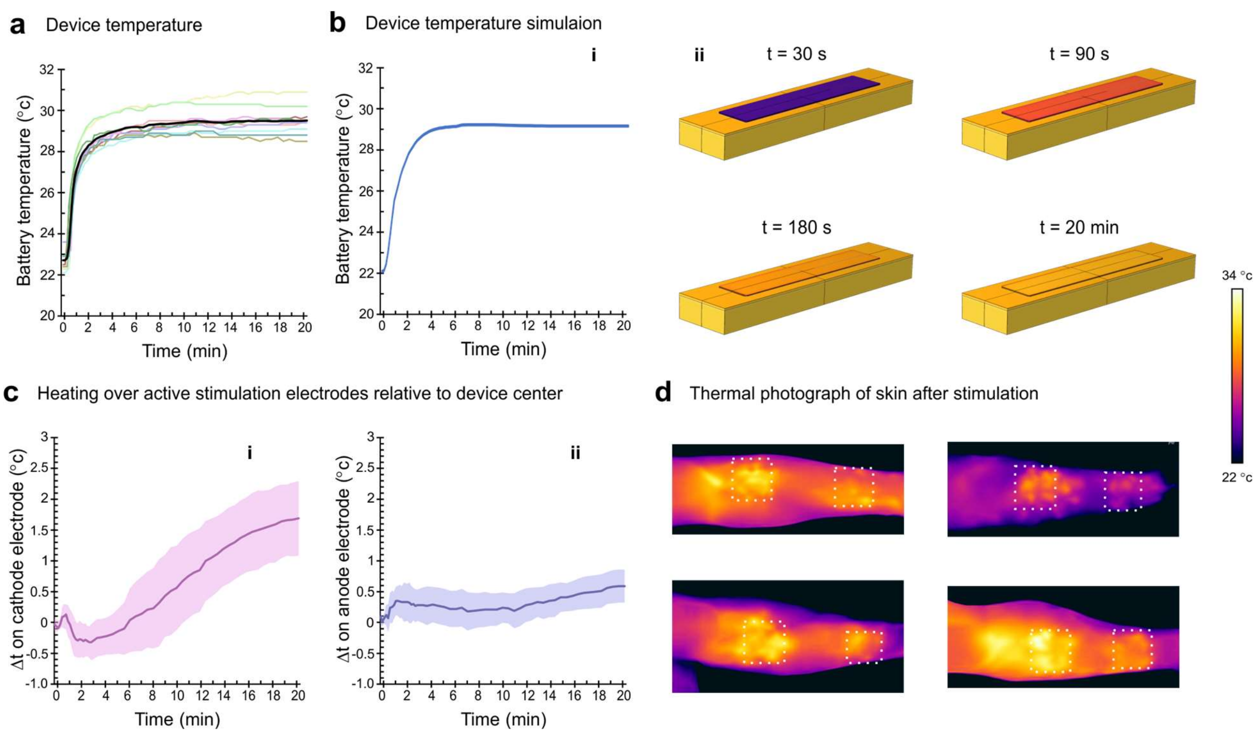

Supplementary Figure 1 | Temperature Transition of exemplary Wearable Disposable Electrotherapy device. Device temperature quickly warms to skin temperature by placement on subjects' skin (t=0). **a)** Battery pack temperature measured using sensors in place of battery active material in interface test devices for 10 subjects (colored lines) and average (black line). **b)** FEM bioheat simulation of battery pack temperature. **c)** Relative heating of battery material over stimulation cathode electrode (i) and over stimulation anode electrode (ii), normalized to temperature in the center of device (solid lines: average; shaded areas: variance). **d)** IR thermography of skin after stimulation showing relative heating of skin under cathode (left) and anode (right) stimulation electrodes.

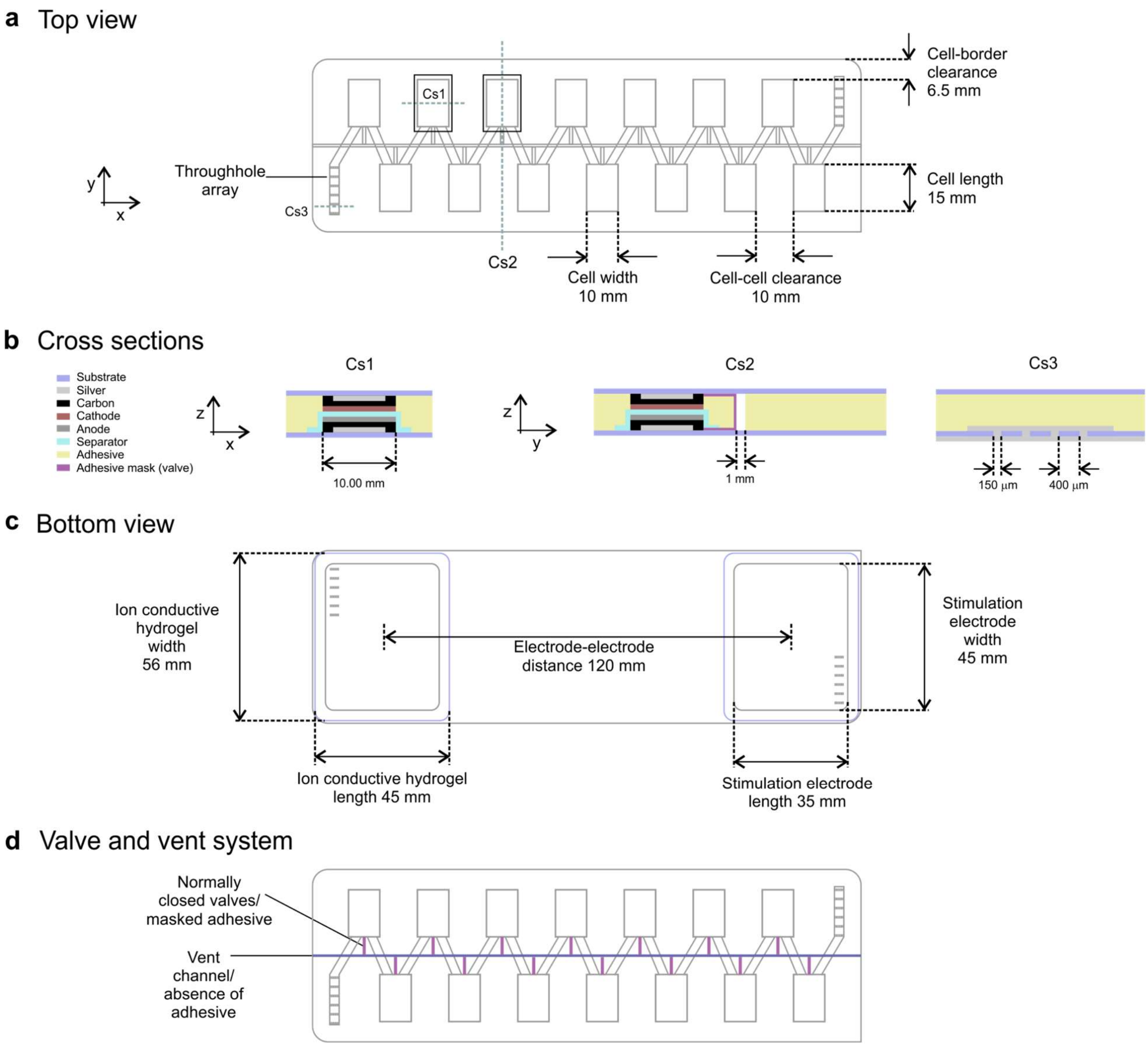

Supplementary Fig. 2 | Geometry of exemplary Wearable Disposable Electrotherapy device (battery pack structure and interconnects, interfaces, venting system). **a)** Device top view showing electrochemical architecture of series cells leading to battery pack terminals (with interconnects to bottom substrate), and integrated venting system. **b)** Device cross sections at battery cell (Cs1), at throughholes (Cs3) and at middle of device (Cs2) showing materials and vent channel (false color legend). **c)** Device bottom view showing interface components with throughhole interconnects to top substrate. **d)** Device cross section highlighting venting system.

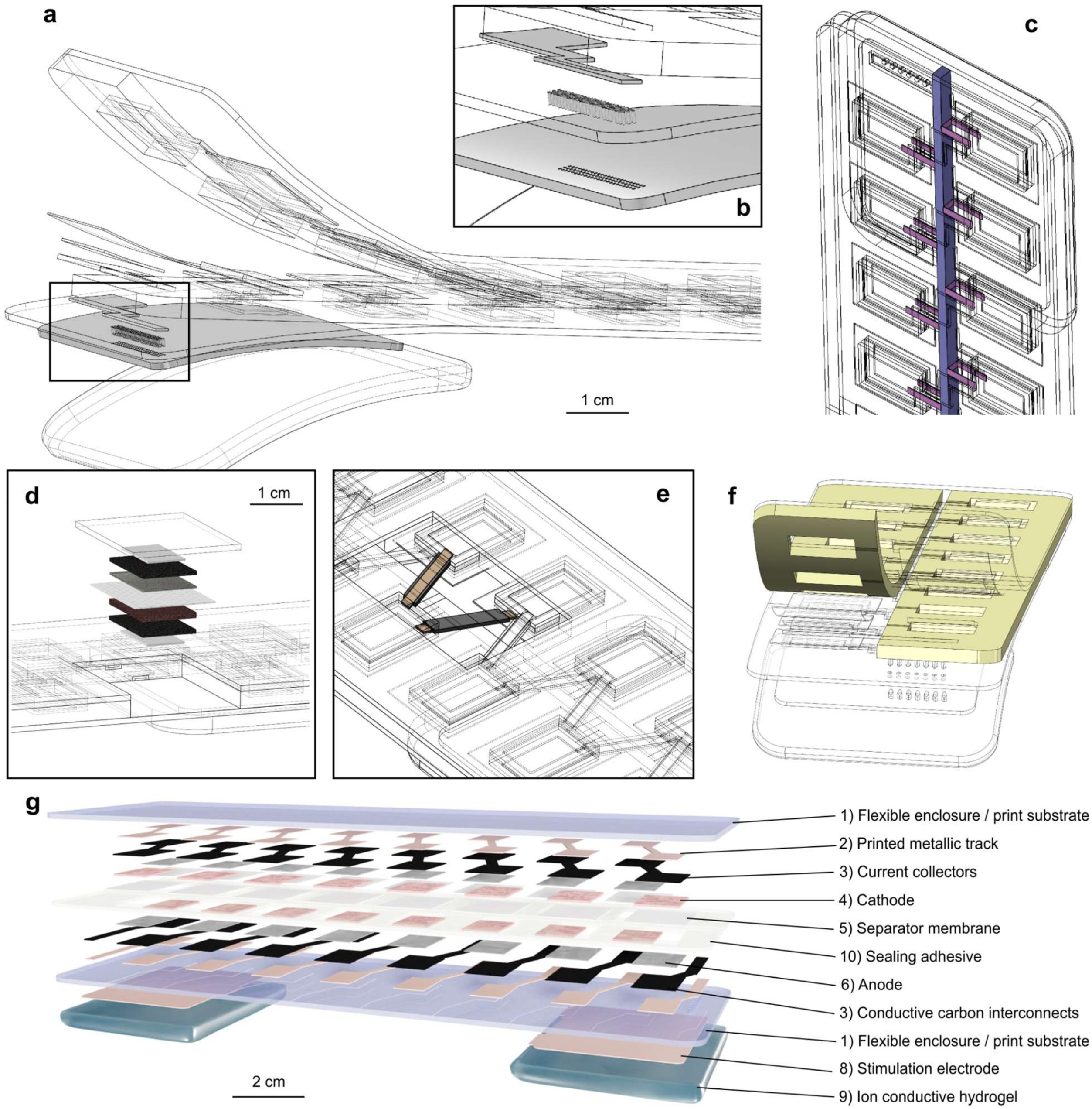

Supplementary Fig. 3 | 3D Geometry of exemplary Wearable Disposable Electrotherapy device. a) Exploded view of device with **b)** Inset showing array of holes on the substrate filled with conductive material, connecting stimulation electrode on back of the substrate to the interconnect on the top of the substrate. **c)** Areal geometry showing the venting system. The vent channel (negative space) is shown in blue and normally closed valves are shown in purple. **d)** Exploded view of layers of one battery cell (top to bottom: substrate enclosure, silver conductor, carbon current collector, anode, separator, cathode, carbon current collector, silver conductor. **e)** View of two interconnects (one on bottom and one on top substrates) connecting one battery cell to two adjacent cells. **f)** Two strips of double-sided tape with cutouts for battery cells, and narrow strips of adhesive masking. The 1 mm gap between adhesives forms the vent channel. **g)** Exploded device view with indexed design elements.

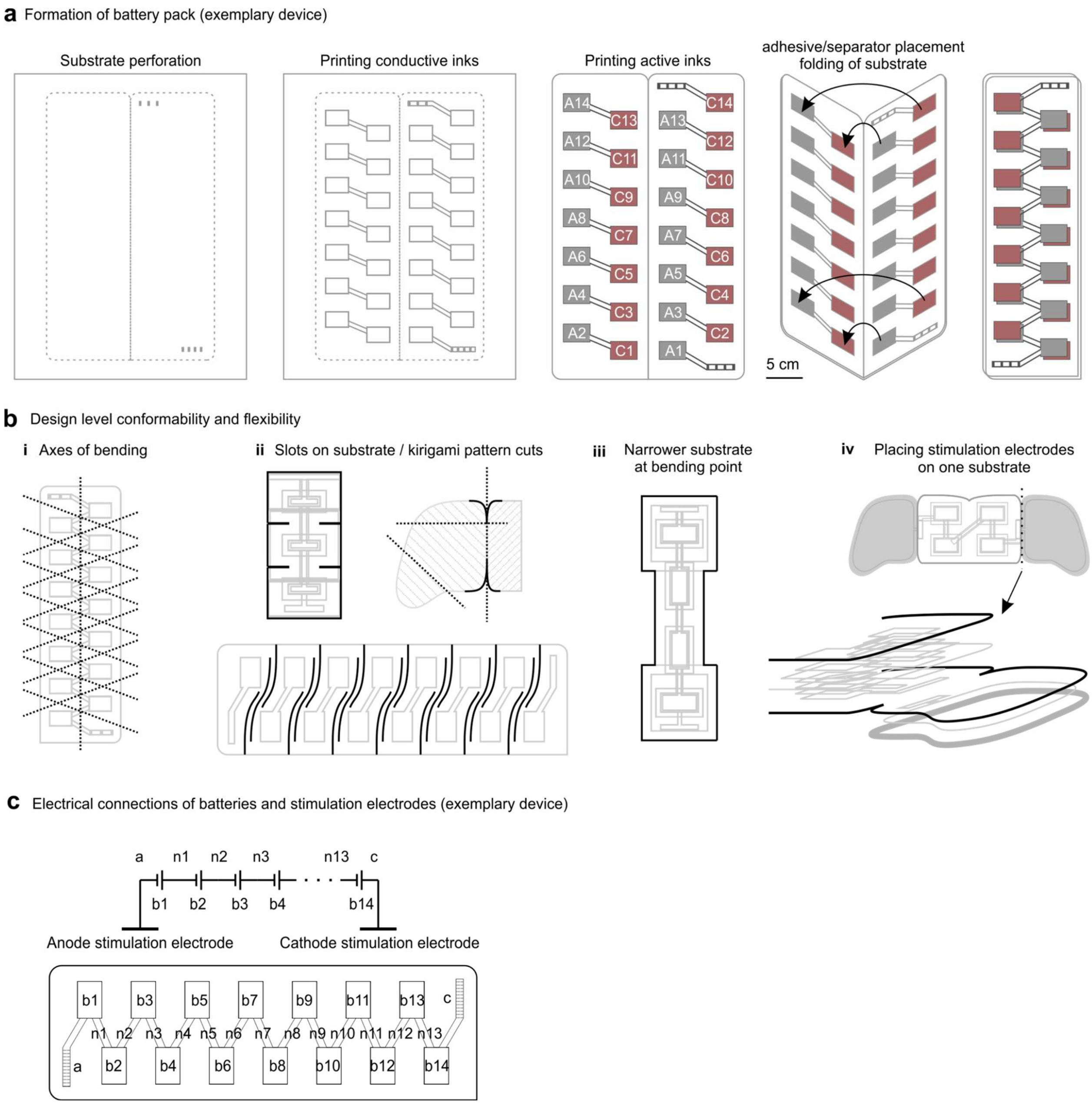

Supplementary Fig. 4 | Formation of 3D structure and battery pack functionality of Wearable Disposable Electrotherapy device. **a)** All components, including interconnect and active materials (forming cell pairs, numbered), are printed on a single substrate. In the final manufacturing steps separators and adhesive are added and the device folded, whereby battery cells are formed and connected. **b)** Per application specific requirements, geometry designs further support conformability along low flexural rigidity axes (i), using pattern cuts (ii), and variations in device width (iii) or thickness (iv). **c)** The battery pack output at the terminals (a: stimulation anode, c: stimulation cathode) reflects the series output of battery cells (b1 to b14) through interconnects (n1 to n13).

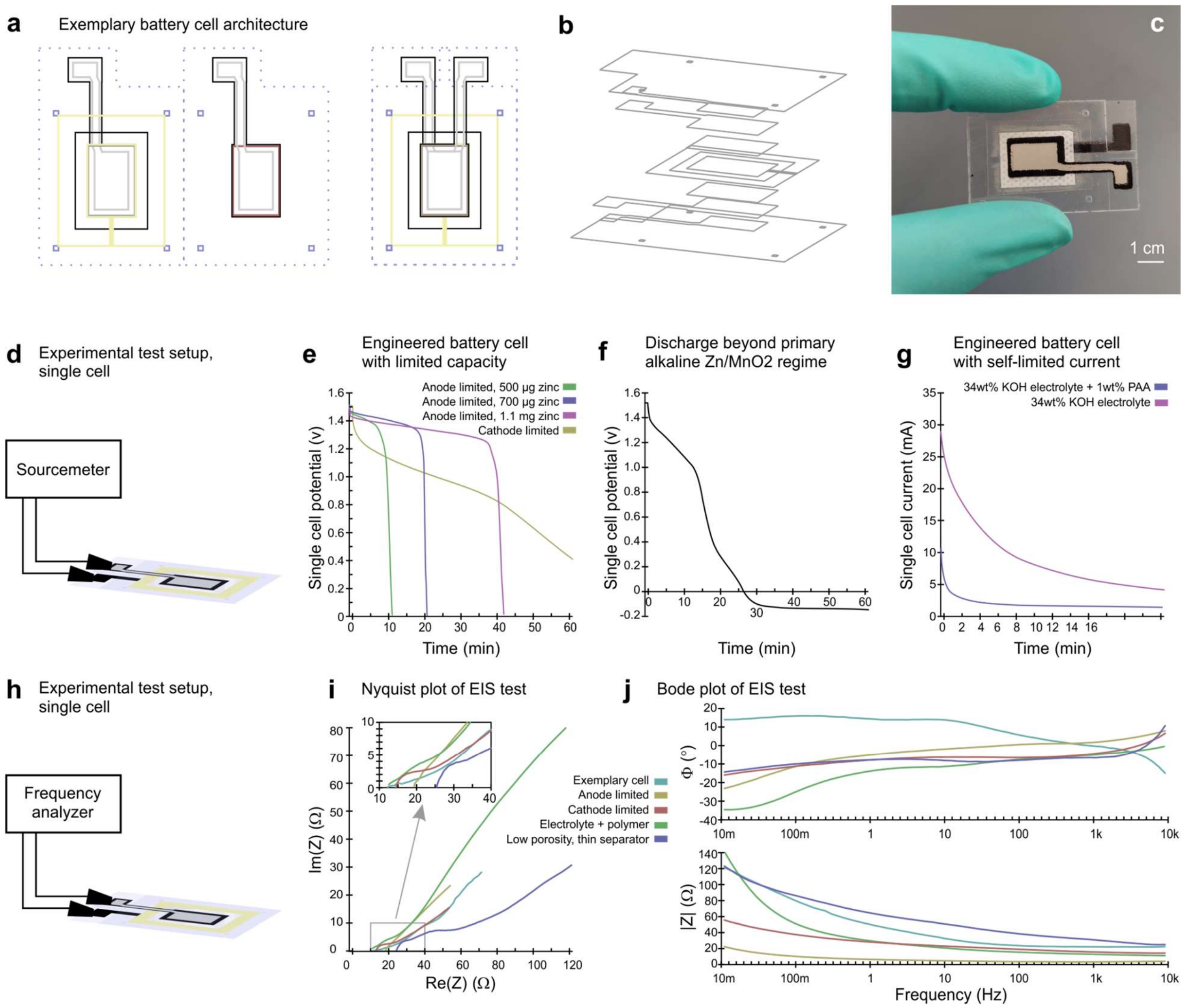

Supplementary Fig. 5 | Single battery cell designs (time/current self-limited) and verification. a) Design of single packaged cell with interconnects for battery discharge and electrochemical impedance tests. **b)** Exploded view of layers of single cell test device. **c)** Photograph of a single cell test device. **d)** Experimental test setup for a single cell test device discharge test. **e)** Discharge curves for single cells under 700 µA constant current. Note the flat discharge curve followed by sudden drop in anode limited battery vs discharge curve of cathode limited battery. In anode limited batteries, total capacity of the battery is controlled by the mass of zinc. **f)** Discharge curve of a printed battery beyond 0.9 v to predict interaction with load. **g)** Discharge curves for single cells connected to 33 Ω constant load. High current (peak and average) during discharge resulted from a typical cell. Flat discharge and low current rate for a cell with similar mass of active materials with additional current limiting mechanism. Note maximum discharge current can be self-limited independent from load value. **h)** Experimental test setup for a single cell test device electrochemical impedance spectroscopy (EIS). **i)** Nyquist and **j)** Bode plot of electrochemical impedance spectroscopy performed potentiostatically at open circuit voltage with a small signal stimulus of 5 mV across 10 mHz - 10 kHz frequency range.

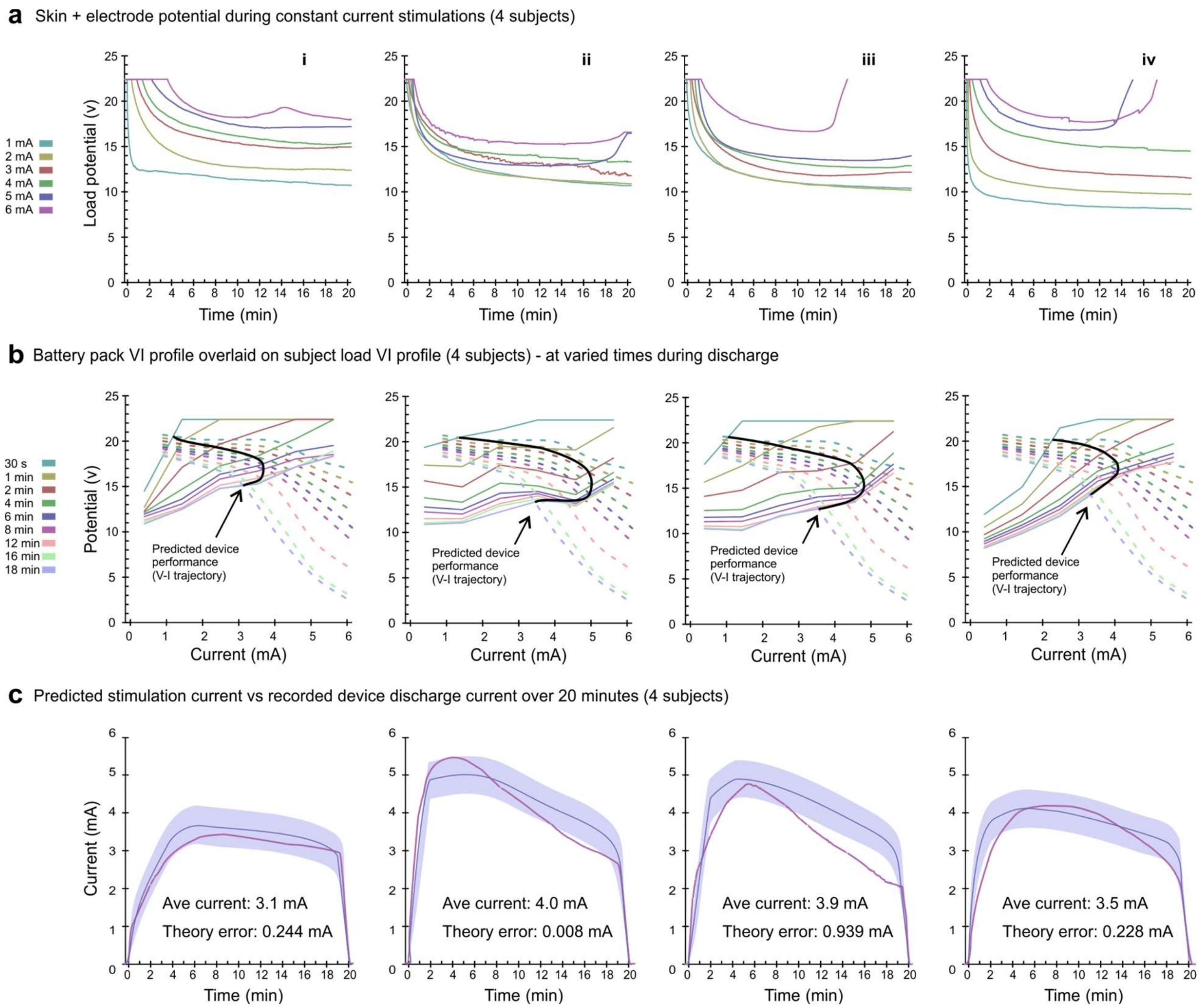

Supplementary Figure 6 | Accurate subject-wise simulation of exemplary Wearable Disposable Electrotherapy device performance. a) Interface-physiological load test results for 4 subjects under constant current stimulation at amplitudes of 1-6 mA and voltage limit of 22.4 v during 20 min. **b)** The associated isotemporal V-I profile of subject-specific interface-physiological load results (colored solid lines) are overlaid with exemplary device battery pack V-I performance (colored dashed lines). Battery pack data is from separately-collected galvanostatic discharge tests (1-6 mA, 20 min). The overlaid interface-physiological load and battery pack V-I profiles are represented for varied time points during discharge (colors). At each timepoint, the intersection of these V-I plots reflects source-load coupling (see Isotemporal-Trajectory theory Supplementary Notes 1). The interpolation through these intersections (solid black line) is then the simulated device discharge trajectory. **c)** This predicted discharge trajectory is re-plotted as current over time performance (blue lines). On a subject-wise basis, this illustrates the design / simulation approach developed for Wearable Disposable Electrotherapy devices, and is then validated. Once built according to theory, Wearable Disposable Electrotherapy exemplary devices were discharged across subjects the experimental current recorded; shown for four subjects (purple lines). The average current per subject is indicated, and is within the exemplary device target (3 ± 1 mA average over 20 min). The blue shaded region indicates 500 μA error from theory, and average error per subject is indicated.

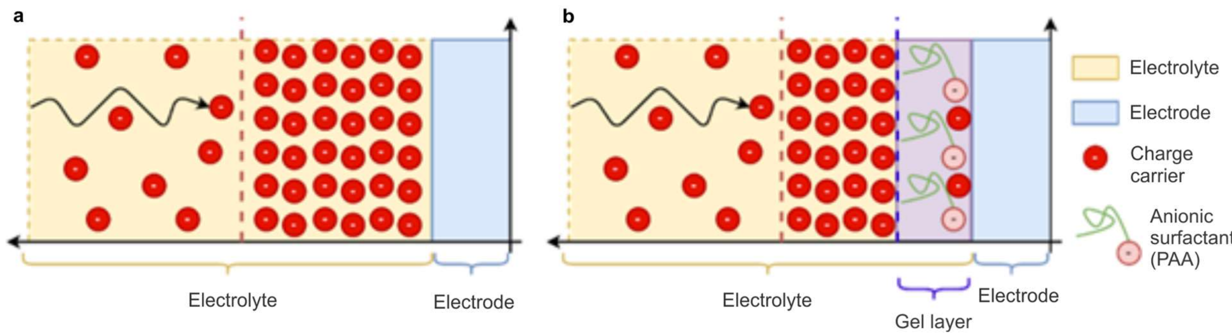

Supplementary Figure 7 | Current self-limiting mechanism by addition of polymer in battery electrolyte. Schematic of charge carrier transport to electrode surface in **a)** electrolyte without polymer additive, resulting in high current delivery capacity of cell; and **b)** electrolyte with specific proportion of polymer additive. Mechanistically, PAA impedes the cell's operating current at two scales (55). At large scale, increased viscosity of electrolyte impedes the diffusion of charge carriers, in addition to competitively adsorbing to the surface of the electrode. On the molecular scale, PAA de-protonates leaving a negatively charged carboxylate group under alkaline conditions (56), this limits the number of charge carriers available for redox at the electrode surface. This technique is one of the tools presented in this work to implement a self-limited mechanism for Wearable Disposable Electrotherapy.

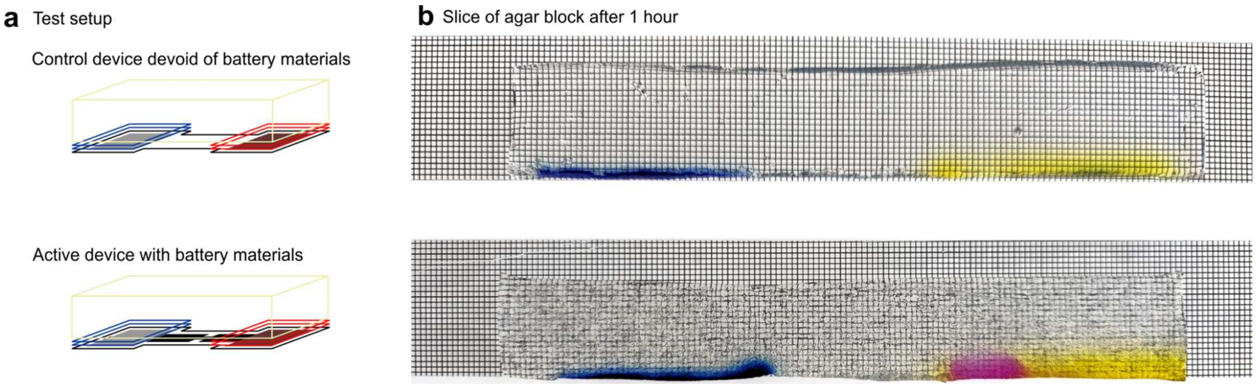

Supplementary Figure 8 | Performance of iontophoresis application Wearable Disposable Electrotherapy device on a skin phantom. (a) Experimental set-up to evaluate enhanced ionic delivery. (b) Top row shows passive diffusion of dyes into phantom placed on the electrodes of a control device (devoid of battery materials). Bottom row shows enhanced dye movement due to iontophoresis, demonstrating the device's efficacy in facilitating active transport of charged molecules. 0.8 ml of 0.14% Phenol Red (negatively charged, molecular weight 354.4 g/mol) was applied to the nonwoven felt placed on the negative stimulation electrode, and 0.8 ml of 0.2% Methylene Blue (positively charged, molecular weight 319.9 g/mol) was applied to positive stimulation electrode. The phantom blocks were prepared using 250 g of deionized water, 2.5 g of agar powder, and 250 µg of NaCl. The blocks were placed on both the control and active devices for two hours, then sliced and placed on a grid with 1 mm spacing between lines to visualize dye diffusion.

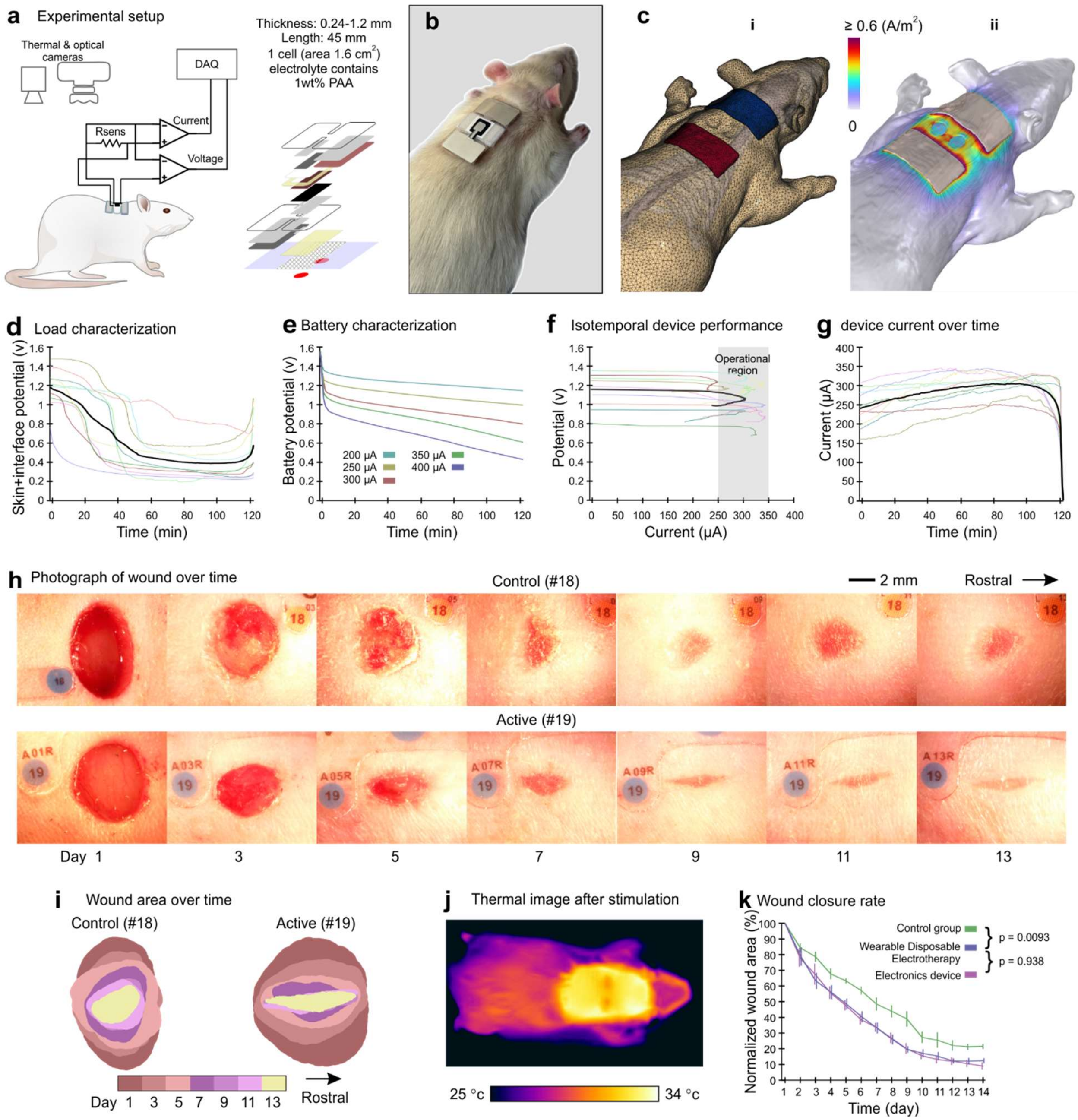

Supplementary Figure 9 | Accelerated wound healing in a rodent model by Wearable Disposable Electrotherapy. a) Experimental setup and wound healing device for rodents. **b)** Photograph of device on rat. **c)** FEM simulation of current delivery across a wound. **d)** Load impedance. Individual subjects (colored lines) and average (black lines). **e)** Discharge of battery cells. Current output during application for rat wound healing; V-I **(f)** and over time **(g)**. **h)** Exemplary images of wound healing in control and active Wearable Disposable Electrotherapy conditions and **i)** wound closure over time. **j)** Thermal image of stimulation. **k)** Rate of wound healing in the control (n=3), Wearable Disposable Electrotherapy (n=4), and electronics-based stimulation groups (n=4) (mean ± SEM). The interaction between the treatment group and time was significant ($p < 0.001$). Post-hoc pairwise comparisons revealed that wounds in the Wearable Disposable Electrotherapy group healed significantly faster than control (estimate = 14.69, SE = 3.70, $t(8.39) = 3.973$, $p = 0.009$). No significant difference in wound healing rates was found between Wearable Disposable Electrotherapy and electronics-based active stimulation (estimate = 1.44, SE = 4.24, $t(8.39) = 0.341$, $p = 0.938$).

Supplementary Table 1 | Material use of Wearable Disposable Electrotherapy vs. conventional electrotherapy consumables.

	Wearable Disposable Electrotherapy				Consumable components of conventional electrotherapy	
Material	Exemplary	tDCS	iontophoresis	Wound healing	AA battery	Disposable electrode (x2)
Conductive Hydrogel	4.05 g	3.96 g	-	1.2 g		~4 g
Nonwoven / Sponge	-	-	0.56 g	-		0.5-2 g
Plastic substrate	2.80 g	1.93 g	1.24 g	0.35 g		~4 g
Adhesive	1.885 g	888 mg	983 mg	340 mg		~1.5 g
Separator	111 mg	45 mg	40 mg	35 mg	600 mg	
Electrolyte	196 µl	150 µl	152 µl	42 µl		
Copper ink[1]	76.1 mg	22.6 mg	37.8 mg	11.1 mg		
Carbon ink[1]	122.3 mg	38.2 mg	25.8 mg	7.8 mg		
Anode material[1]	373.8 mg	170.9 mg	142.4 mg	27.7 mg	5.2 g	
Cathode material[1]	756 mg	345.6 mg	288 mg	56.2 mg	12.3 g	
Solid Metal parts	-	-	-	-	4.6 g	0.6-2 g

[1] Weight of inks measured after drying.

Supplementary Notes 1 – Theoretical Framework

Elucidating the dynamics of a system comprised of two coupled subsystems, in our case, the battery pack and load, is part of a class of problems addressed in dynamical systems theory (1,2,3). Our device formulation and procedures are part of a framework for extracting information on the dynamics of the physiological load. The theoretical framework on which this is based is presented here.

1.0 – Isotemporal Trajectory Framework Overview

In this supplementary Notes, we characterize the Wearable Disposable Electrotherapy device performance (considered a coupled system of the battery pack on the load) using a closed-form simulation of uncoupled parts (Section 3.0). We base these analyses on the independently measured dynamic (temporal) behavior of each part (battery pack and load) (Section 2.0) - this parameterization is essential since the goal of the analysis is to predict performance of a specifically designed (sized) battery pack on an associated interface-physiological load, modeling and so accounting for individual variation. These results further explain the current regulation theory of Wearable Disposable Electrotherapy (unlike any prior electrotherapy or battery technology).

The specific closed-form simulation steps are demonstrated graphically (Section 4.2). This theory is part of the device design process, specifically the battery sizing stage (Figure 2). We demonstrate the parameters from the two uncoupled sub-systems can be solved uniquely, resulting in the operating line of the coupled system (i.e. the trajectory).

2.0 – Battery Pack and Load as Uncoupled Dynamical Systems

In our device design approach, we identify two subsystems: the battery pack (B) and the load (L). First, we consider these two subsystems independently (i.e., without interactions). The voltages V_B and V_L of the battery (B) and load (L), respectively, are response functions, $\{f_A, f_B\}$, of time, t, and electrical current I_n, shown in Eqns. (S1) – (S2):

$$\frac{dV_B}{dt} = V_{B,t} = f_B(\alpha_B, e_B) \tag{S1}$$

$$\frac{dV_L}{dt} = V_{L,t} = f_L(\alpha_L, e_L) \tag{S2}$$

where I_n is a constant current stimulus, α_B and α_L are internal parameters of each system (i.e., controllable during design stage; e.g. battery pack features such as number of cells, cell geometry, gel/battery chemistry); while e_B and e_L are environmental factors (i.e., not controllable by design procedure; e.g. presence of skin products, humidity, working temperature, …) affecting each subsystem. These parameters also have temporal dependency.

Experimentally, by independently connecting the battery packs and load to a sourcemeter, with varied constant current levels (e.g., $I_n = 1\, mA, 2\, mA, \ldots$), and measuring the associated output voltages (V_B, V_L), the response functions of each system are determined (i.e., f_B and f_L).

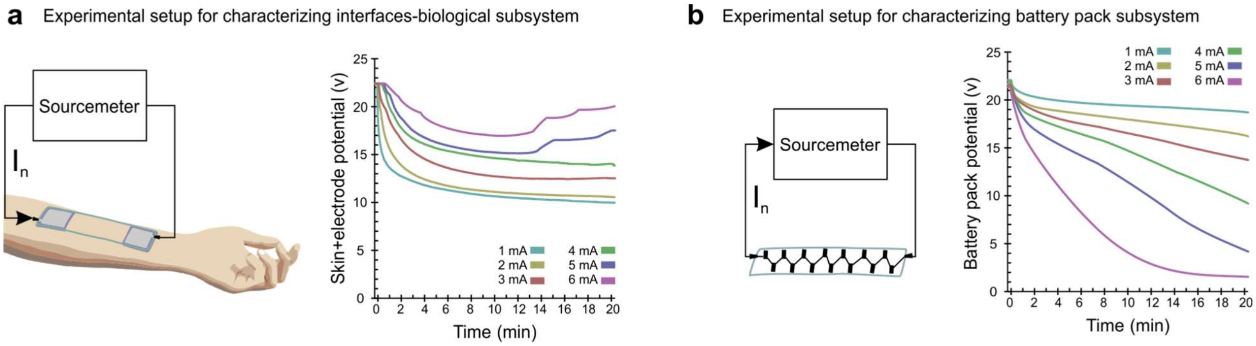

Supplementary Figure 10 | Battery Pack and Load as a Coupled Dynamical System

During the device operation, the two subsystems, battery pack and load are physically coupled, resulting in a coupling discharge between the subsystems. The voltage and current of each part of the system evolves with the following response functions in Eqns. (S3) – (S4):

$$\hat{V}_{B,t}(t) = \hat{f}_B(\alpha_B, e_B) \qquad (S3)$$

$$\hat{V}_{L,t}(t) = \hat{f}_L(\alpha_L, e_L) \qquad (S4)$$

The essential difference between the two dynamical expressions for the coupled dynamical system and the decoupled system (Section 2.0) is that the actuation or control variable, in this case, the current I_n , is not controlled when the systems are coupled but now represents another state parameter of the coupled system as $I(t)$, as illustrated in Supplementary Fig. 11 due to the absence of a sourcemeter to control the current:

Supplementary Figure 11 | **a)** Characterization of two subsystems using step function I_n **b)** Direct interaction of two subsystems over time resulting in dose current

Since we know these two parts are both in series and parallel with no other branches in the experimental setup, the following condition holds in Eqn. (S5):

$$\hat{V}_B = \hat{V}_L = \hat{V} \qquad (S5)$$

Now we develop an approximation that allows for a closed-form solution by first taking a Taylor expansion of (S3) – (S4) around the currents from the decoupled sub-systems (Section 2.0), shown in Eqns. (S6) – (S7). Note, that in the expansion of Eqn. (S6), all positive terms drop since energy is dissipated into the load (L) from the battery (B). Conversely, all negative terms in the expansion of Eqn. (S7) drop. This is evidenced in Supplementary Figure 11, which indicates the values of derivatives at higher orders.

$$\hat{V}_{B,t} \cong \hat{f}_B(\alpha_B, e_B) + \frac{\partial \hat{V}_{B,t}}{\partial I}(I(t) - I_n) + O\left(I^2(t)\right) \tag{S6}$$

$$\hat{V}_{L,t} \cong \hat{f}_L(\alpha_B, e_B) + \frac{\partial \hat{V}_{L,t}}{\partial I}(I(t) - I_n) + O\left(I^2(t)\right) \tag{S7}$$

However, by invoking Eqn. (S5) to simplify the response functions of the coupled subsystems and truncating the Taylor series in Eqns. (S6) - (S7) by assuming when $|I(t) - I_n| << 1$ or $I(t) \approx I_n$, we can simplify them as shown in Eqns. (S8) - (S9). A Taylor expansion of Eqns. (S1) - (S2) are also taken as shown in Eqns. (S10) - (S11). In Eqns. (S8) - (S11), an integration is taken over time where the integration constants of each sub-system's voltage are represented as a function of its initial condition.

$$\hat{V}_B \cong \int \hat{f}_B(\alpha_B, e_B)\,\partial t + \hat{g}_B\left(\hat{V}_{B0}\right), \qquad \hat{V}_B(t=0) = \hat{V}_{B0} = V_{B0} \tag{S8}$$

$$\hat{V}_L \cong \int \hat{f}_L(\alpha_L, e_L)\,\partial t + \hat{g}_L\left(\hat{V}_{L0}\right), \qquad \hat{V}_L(t=0) = \hat{V}_{L0} = V_{L0} \tag{S9}$$

$$V_B \cong \int f_B(\alpha_B, e_B)\,dt + g_B(V_{B0}), \qquad V_B(t=0) = V_{B0} = \hat{V}_{B0} \tag{S10}$$

$$V_L \cong \int f_L(\alpha_L, e_L)\,dt + g_L(V_{L0}), \qquad V_L(t=0) = V_{L0} = \hat{V}_{L0} \tag{S11}$$

The initial conditions for each sub-system when decoupled is taken to be equal to the initial conditions of the system when coupled. For instance, the initial voltage of the battery, V_{B0}, is the same under open-circuit conditions (decoupled from the load) and when coupled to the load at time $t = 0$, and likewise for the load.

By taking the differences in the coupled and decoupled voltages for the battery under these conditions (i.e., the difference between Eqns. (S8) and (S10)) since it is the subsystem whose response function we ideally know, and derive the following Eqn.

$$\hat{V}_B - V_B = \int \left[\hat{f}_B(\alpha_B, e_B) - f_B(\alpha_B, e_B)\right]\,dt + \left[\hat{g}_B\left(\hat{V}_{B0}\right) - g_B(V_{B0})\right]$$

The last two terms in the brackets correspond to initial conditions of the battery when coupled and decoupled, which equate to zero according to Eqns. (S8) and (S10).

$$\left[\hat{g}_B\left(\hat{V}_{B0}\right) - g_B(V_{B0})\right] = 0$$

Following this procedure, Eqns. (S12) - (S13) can then be derived as follows and simplified using Eqn. (S5):

$$\hat{V} - V_B = \int \left[\hat{f}_B(\alpha_B, e_B) - f_B(\alpha_B, e_B)\right] dt \tag{S12}$$

$$\hat{V} - V_L = \int \left[\hat{f}_L(\alpha_L, e_L) - f_L(\alpha_L, e_L)\right] dt \tag{S13}$$

In both Eqns. (S12) - (S13), the current is a known constant for each response in the integrands. To fully close this system of equations to determine the unknown response functions of the load, $\{\hat{f}_B, \hat{f}_L\}$, we can set $\hat{V} - V_B = \hat{V} - V_L = 0$. This implies $\hat{V} = V_B$ and $\hat{V} = V_L$, and therefore $V_B = V_L$. With respect to the response functions, it allows us to express the response functions of each subsystem in the integrand as follows in Eqn. (S14):

$$\hat{f}_L(\alpha_L, e_L) = \hat{f}_B(\alpha_B, e_B) = f_B(\alpha_B, e_B) = f_L(\alpha_L, e_L) \tag{S14}$$

These conditions are satisfied by the isotemporal curves (e.g. Figure 5f and Supplementary Figure 11), where the surfaces represent response functions of battery pack and load while intersection gives us information on the response function of the interaction between them. To summarize, the following criteria permit the closed-form approximation:

$$|I(t) - I_n| \cong 0 \;\Rightarrow I(t) \cong I_n$$

$$\hat{V} - V_B = \hat{V} - V_L = 0 \Rightarrow \left\{\hat{V} = V_B, \hat{V} = V_L, V_B = V_L\right\}$$

Based on the data gathered from testing of the isolated battery pack and load, the solution used for prediction of the dynamic behavior of the coupled system was empirically derived (section 2.0). We next show graphically how to explicitly implement this closed-form solution (section 4.0).

4.0 - Closed-Form Solution of Simulated Coupled Subsystems

The closed-form solution can be developed using methods ranging from first-principles modeling (i.e., knowledge of the system) to data-driven fitted parametric models. Although conventional model-informed approaches have been developed for both batteries and physiological loads (4-11), a data-driven approach can be used to generate models whose parameters may or may not have physical meaning or are non-parametric. The latter can be implemented in the form of a Lagrange interpolation polynomial (12-14) which results in a unique solution demonstrating the closed-form approximation (Section 2.0 - 3.0).

4.1 - Model of Battery Pack & Load

A model can be developed using only the data set generated from the experiment using an interpolation method, such as the Lagrange interpolation polynomial (12-14). The response functions for the battery pack and load can be represented by a 2D Lagrange interpolation polynomial using Eqn. (S15). $V(I_i, t_j)$ is our experimental data representing the response function as a surface I_i is the i^{th} current data point corresponding to the set of $\{I_n\}$ or constant currents (Section 2.0 - 3.0), and correspond to j number of data points sampled in time. The total number of discrete currents and points sampled in time are k and m, respectively.

$$V(I_i, t_j), \qquad I_i \in \{I_n\}, \qquad t_j \in \{t_0, t_1, \dots, t_m\}, \qquad n = 0,1,2,\dots,k \tag{S15}$$

Using this discrete data set, a 2D Lagrange interpolating polynomial can be constructed by Eqn. (S16), where $L_i(t)$ and $M_j(t)$ are the 1D Lagrange basis polynomials, which across the sum leads to a polynomial of order $(k-1)(m-1)$ that considers the whole data set, and $P(I, t, V(I_i, t_j))$ is the Lagrange polynomial that models the dataset.

$$P\left(I, t, V(I_i, t_j)\right) = \sum_i \sum_j V(I_i, t_j) L_i(I) M_j(t) \tag{S16}$$

Together, they can be equated to identify the intersection points of the response functions of the battery pack and physiological load by solving (the roots of a polynomial), as shown in Eqn. (S17):

$$P_L\left(I, t, V_L(I_i, t_j)\right) - P_B\left(I, t, V_B(I_i, t_j)\right) = 0 \tag{S17}$$

4.2 - Closed-Form Prediction of Coupled System Discharge

Following from the relationships between V_B, V_L and $\hat{V}$ (Section 3.0), a final closed-form model is developed by finding the intersection of two subsystem's response functions. To define the intersection, a Lagrange polynomial can be used to find the set of voltages, currents and times resulting in a determined set of intersection points, which can then be fitted to further define the isotemporal curve as demonstrated in Supplementary Fig. 12. The isotemporal trajectory theory can be used to simulate the performance of varied battery pack designs (Fig. 2) across subject-specific loads during the battery pack sizing stage.

5.0 - Universal Device from Individually Precise Simulations

In order to design a Wearable Disposable Electrotherapy device for a specific application considering the subject variability, first the target population's impedance spectrum and distribution are collected (impedance profiling). In the next stage, an initial prototype is designed by using average impedance. Population-wide simulation is then done using Isotemporal Trajectory Theory (using individual impedances) verifying performance of a single optimized device design across individuals. This approach also allows for simulation of devices on any custom (synthetic) load. After the final stage of device validation, the recorded output of the Wearable Disposable Electrotherapy device for each subject can be compared to their simulated performance (Supplementary Fig. 6c), providing further support for Isotemporal Trajectory Theory.

Voltage response function under constant-current stimulus for tested current values

Our novel theoretical framework and the illustrated numerical solution are in principle independent of scales. For the conventional applications demonstrated in this report the scales for volts (voltage), mA (current), minutes (time).

Fitted surface to the voltage response function under constant-current stimulus

Iso-temporal lines (red/blue) at selected time points, fitted on surface.

Intersection of plains is indicated as thick black line. This intersection indicates the simulated output of the coupled systems

Rotated view of voltage response along time axis (lines for tested current values are not shown)

Iso-temporal response for selected time points (fitted surface is removed)

Iso-temporal response for selected time points (2-D view overlaid lines for selected time points)

The right panel shows iso-temporal response functions for both subsystems and their intersection. This resultant is the simulated device output of the coupled sub-systems.

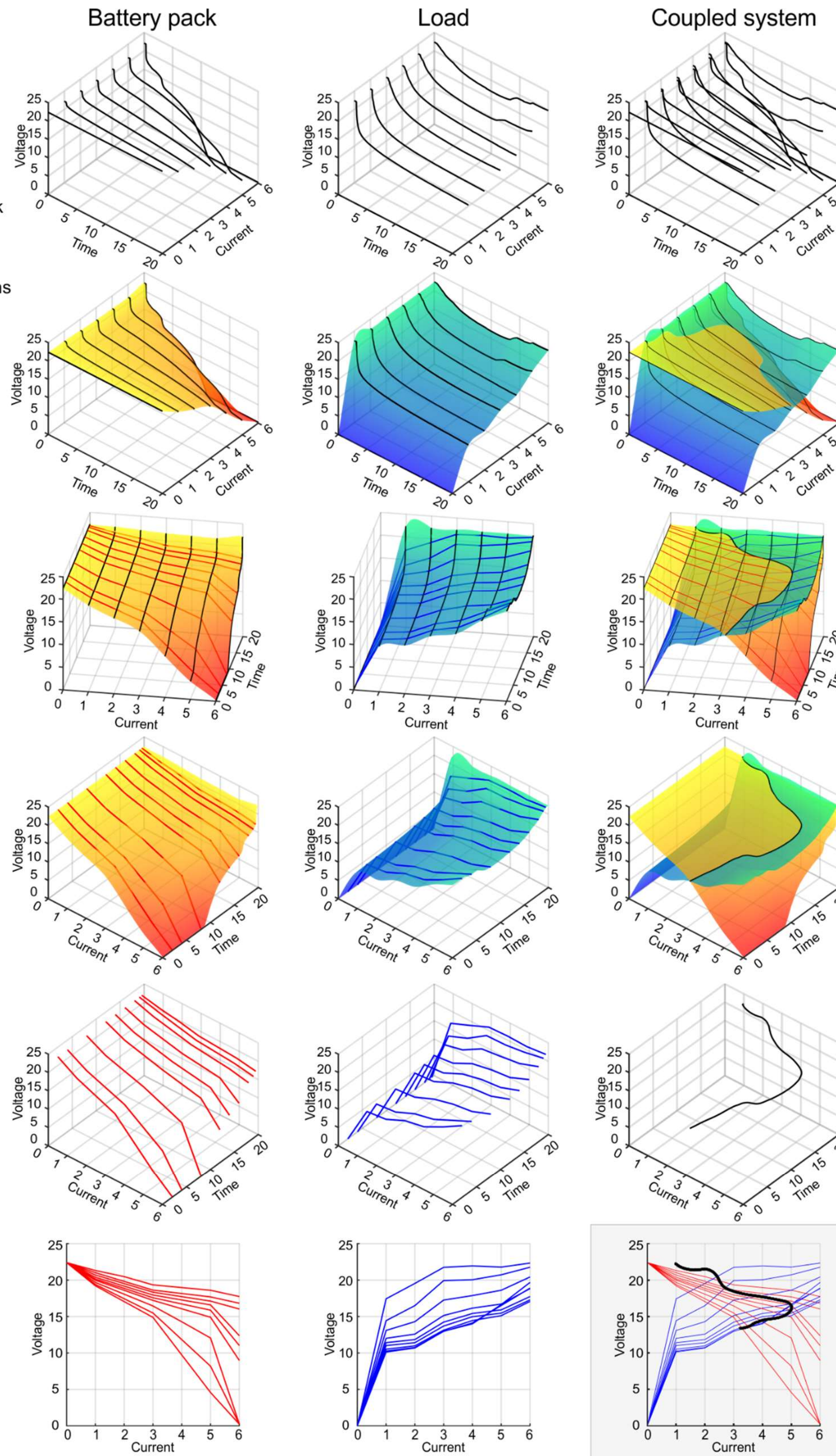

Supplementary Figure 12 | Isotemporal Trajectory Theory predicts the interaction of subsystems by determining intersection of them in a 3D space.

Supplementary Notes 1 References

1. Sjövall, P. and Abrahamsson, T., 2008. Substructure system identification from coupled system test data. Mechanical Systems and Signal Processing, 22(1), pp.15-33.
2. D'Ambrogio, W. and Fregolent, A., 2011, February. Direct decoupling of substructures using primal and dual formulation. In Linking Models and Experiments, Volume 2: Proceedings of the 29th IMAC, A Conference on Structural Dynamics, 2011 (pp. 47-76). New York, NY: Springer New York.
3. Liao, X.H., Wu, W.F., Meng, H.D. and Zhao, J.B., 2020. Response prediction and dynamic substructuring for coupled structures in the frequency domain. Journal of Mechanics, 36(6), pp.867-879.
4. Nishida, Y., Sasaki, K., Yamamoto, K., Muramatsu, D. and Koshiji, F., 2019. Equivalent circuit model viewed from receiver side in human body communication. IEEE Transactions on Biomedical Circuits and Systems, 13(4), pp.746-755.
5. Gorbunov, A., Gromov, Y. and Egorov, V., 2019, July. The calculation of the impedance of biological tissue on the model of Yamamoto in the process of galvanic effects. In Journal of Physics: Conference Series (Vol. 1278, No. 1, p. 012037). IOP Publishing.
6. Yamamoto, Y. and Yamamoto, T., 1987. Measurement of electrical bio-impedance and its applications. Medical Progress through Technology: Medical engineering in Japan Research and development, pp.171-183.
7. Seyedi, M., 2024. Biological cell response to electric field: a review of equivalent circuit models and future challenges. Biomedical Physics & Engineering Express.
8. McAdams, E.T. and Jossinet, J., 1996. Problems in equivalent circuit modelling of the electrical properties of biological tissues. Bioelectrochemistry and bioenergetics, 40(2), pp.147-152.
9. Rupnik, M., Runovc, F. and Kordas, M., 2001. The use of equivalent electronic circuits in simulating physiological processes. IEEE transactions on education, 44(4), pp.384-389.
10. Bellia, S.A., Saidane, A., Hamou, A., Benzohra, M. and Saiter, J.M., 2008. Transmission line matrix modelling of thermal injuries to skin. Burns, 34(5), pp.688-697.
11. Cornwall, M.W., 2007. Electrotherapy explained: principles and practice, ed 4. Physical Therapy, 87(8), pp.1088-1088.
12. Moin, P., 2010. Fundamentals of engineering numerical analysis. Cambridge University Press.
13. Sauer, T. and Xu, Y., 1995. On multivariate Lagrange interpolation. Mathematics of computation, 64(211), pp.1147-1170.
14. Cuevas, E., Luque, A. and Escobar, H., 2023. Interpolation and Polynomials. In Computational Methods with MATLAB® (pp. 77-101). Cham: Springer Nature Switzerland.

Supplementary Notes 2 - Scalable Manufacture

The manufacturing process for Wearable Disposable Electrotherapy devices adapts methods for economic efficiency and high volume (Supplementary Fig. 13). These processes are characterized by subtractive and additive approaches to produce an enabling 3D device structure (Supplementary Fig. 13b, Supplementary Fig. 4a).

Fabrication begins by heat treating the substrate to ensure its physical stability. This treated substrate serves as the foundation for the deposition of the components that will comprise the electrotherapeutic device. The substrate undergoes rinsing (e.g. water + detergent) to remove contaminants that can affect the adhesion of the components that will be printed onto the substrate. Plasma treatment modifies the substrate's surface energy, increasing the polarity of the polymeric substrate, and thus enhancing the ink adhesion and ensuring effective sealing in the downstream processes.

The conductive pathways required by device design are formed by printing conductive and dielectric inks providing required functionalities. Copper ink, conductive carbon ink, zinc ink, Ag/AgCl ink and dielectric ink are among the materials used to construct the various elements of the device. Each fabrication stage is followed by drying and baking steps to set the features in place. After forming these features, the battery anode and cathode materials are deposited on the battery current collectors. Electroplating (for microgram accuracy in the deposition of active materials), screen printing (for thinner layers), and/or stencil printing (for controlled deposition thickness, favorable for cathode deposition) were applied for additive manufacture of device layers. The selected inks formulation supports air-stable production, with ink rheology optimized for the printing method while achieving the electrical performance required such as discharge rate. We use a compaction process to increase electrode density that leads to decreased internal battery resistance for the cathode material.

We use a parallel plate battery structure where a separator membrane is assembled between the battery electrodes to electrically isolate them while allowing ionic transport. The sealing stage closes the battery pack between the two enclosure sheets with double-sided tape with an adhesive tailored for low surface energy polymer surfaces. During the sealing stage, the venting system is created by selective masking of adhesive (Supplementary Fig. 2b,d and Supplementary Fig. 5c,f). After sealing, electrolyte is introduced to cells resulting in an active, charged battery unit. In the final fabrication step, hydrogel or non-woven felt (later soaked with electrolyte) as stimulation ion-conductive buffer is applied to the outer surface. Supplementary Figure 13c shows the resulting stack of different layers forming the device.

The structure of the battery electrodes and the film uniformity was confirmed by imaging using Scanning Electron Microscopy (SEM) of the deposited layers (Supplementary Fig. 13d). The separator membrane was also imaged using SEM to confirm the absence of defects that could result in short-circuiting a particular cell.

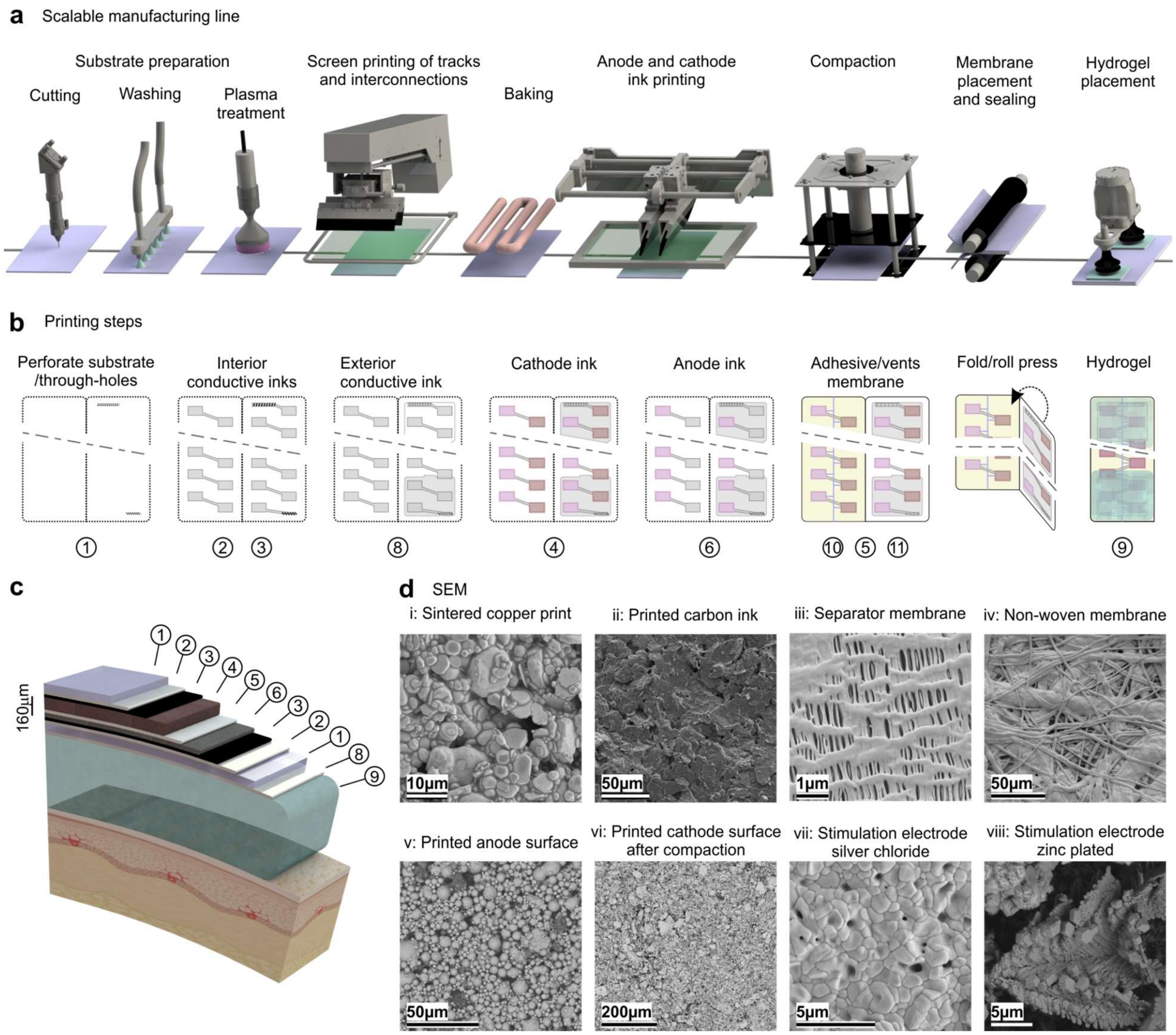

Supplementary Figure 13 | Wearable Disposable Electrotherapy manufacturing processes. **a**) Scalable manufacturing line consists of substrate preparation, printing conductive/resistive and dielectric inks, curing and baking, printing active materials, compacting, membrane placement and sealing and hydrogel placement. **b**) Steps of additive manufacturing on a single substrate leading to 3D device architecture. **c**) Schematic of layers forming the device including printed battery pack, interconnects, interface, and enclosure elements. **d**) SEM of i: sintered printed copper surface, ii: printed conductive carbon ink, iii and iv: surface of porous PP film and non-woven PP film for retaining battery electrolyte as separator or electrolyte bridge, v: printed anode surface, vi: compacted cathode surface vii: corroded surface of printed silver for cathode stimulation electrode, viii: zinc plated surface for anode stimulation electrode. Elements 1-11 labels as per Fig. 1.

Supplementary Notes 3 - Comparison of variability in Wearable Disposable Electrotherapy with Conventional Electrotherapy

We designed Wearable Disposable Electrotherapy for three applications and validated reliability to specifications. In this Supplementary Notes 2 section we consider and compare to the variability expected from conventional electrotherapy for each application.

Variability in electronics-based tDCS results from:1) applied currents vary 400% (1-4 mA; (4)); 2) even for a given current, individual brain electric field varies >250% (1 - 3); and 3) within a session brain electric fields and applied voltage can fluctuate >25% (4), reflecting adapting scalp resistance (5,6). Thus, factors contributing to variability of electronic-based tDCS are greater than variation on Wearable Disposable tDCS dose.

We evaluated the accuracy of an FDA cleared iontophoretic device (Iontopatch Stat 4; which relies on a lithium coin-cell battery) measuring an average charge 35.9 ± 3.5 mA-min with significant current transients as high as 0.78-1.2 mA. Thus, Wearable Disposable Iontophoresis performance was within target charge rating and less prone to transients than the FDA cleared Iontopatch Stat 4. Iontopatch Stat 4 lithium coin-cell provides excessive energy and high energy throughput. In contrast, the optimally-sized battery pack of the Wearable Disposable Electrotherapy iontophoresis self-regulates the energy delivery, thereby suppressing large transient peaks. Beyond the performance advantage, this design also eliminates the environmental burden of disposable lithium batteries.

We also compared the rate of wound healing achieved by Wearable Disposable Electrotherapy to that of electronics-based electrotherapy, using the same daily regime. there was no statistically significant difference (contrast estimate = 1.44, SE = 4.24, $t(8.39) = 0.341$, $p = 0.938$; Supplementary Fig. 8k).

Patient-to-patient variability is universal in medicine including systemic absorption of pharmaceutical and transdermal adoptions of topical therapies. Electrotherapy is no exception given differences in anatomy and physiology. With any therapy, variability is best handled through consideration of the therapeutic window and personalized dose adjustment. Wearable Disposable Electrotherapy prescription can be readily adjusted, just like pharmacotherapy, through the dose regime (e.g. two a day) or devices with distinct unit dose ("strengths"). Thus, Wearable Disposable Electrotherapy is the first electrotherapy with a delivery model that mirrors the prescription and user experience of pharmaceuticals, including how variability is managed.

Supplementary Notes 3 references

1. Datta, Abhishek, et al. "Inter-individual variation during transcranial direct current stimulation and normalization of dose using MRI-derived computational models." Frontiers in psychiatry 3 (2012): 91.
2. Huang, Yu, et al. "Measurements and models of electric fields in the in vivo human brain during transcranial electric stimulation." elife 6 (2017): e18834.
3. Laakso, Ilkka, et al. "Inter-subject variability in electric fields of motor cortical tDCS." Brain stimulation 8.5 (2015): 906-913.
4. Chhatbar, Pratik Y., et al. "Evidence of transcranial direct current stimulation-generated electric fields at subthalamic level in human brain in vivo." Brain stimulation 11.4 (2018): 727-733.
5. Hahn, Christoph, et al. "Methods for extra-low voltage transcranial direct current stimulation: current and time dependent impedance decreases." Clinical Neurophysiology 124.3 (2013): 551-556.
6. Gomez-Tames, Jose, et al. "Effect of microscopic modeling of skin in electrical and thermal analysis of transcranial direct current stimulation." Physics in Medicine & Biology 61.24 (2016): 8825.